

## Modes of mesoscale sea surface height and temperature variability in the East Australian Current

John L. Wilkin<sup>1</sup> and Weifeng G. Zhang<sup>1</sup>

Received 16 March 2006; revised 1 July 2006; accepted 11 September 2006; published 27 January 2007.

[1] Mesoscale variability where the East Australian Current (EAC) separates from the coast is studied using sea surface temperature and surface velocity streamfunction observed by satellite and a regional numerical model. The mean circulation simulated by the model (the Regional Ocean Modeling System (ROMS)) is compared to a high-resolution regional climatology, and the realism of the simulated mesoscale variability is tested by comparison to statistical analyses of the satellite data. Both ROMS and data show spectral peaks in the mesoscale energy band at periods between 90 and 180 days. Complex Empirical Orthogonal Function (EOF) analysis identifies two significant modes of mesoscale variability in the data; an Eddy Mode, for which the variability propagates southwestward along the coast, and a Wave Mode, for which phase propagation is predominantly onshore. The regional model open boundary conditions include only annual and semiannual harmonics of variability so remote mesoscale forcing is absent. The Eddy Mode is represented well in the model indicating this aspect of the circulation results from local instabilities of the flow and that its underlying dynamical process is simulated well. While the observed and modeled Wave Modes have some similarities, their differences suggest the model is deficient in representing westward propagation of mesoscale period variability in the region. Whatever the source of this energy, the orthogonality property of the EOF analysis indicates the Wave Mode does not interact significantly with eddy processes in the EAC separation.

**Citation:** Wilkin, J. L., and W. G. Zhang (2007), Modes of mesoscale sea surface height and temperature variability in the East Australian Current, *J. Geophys. Res.*, 112, C01013, doi:10.1029/2006JC003590.

### 1. Introduction

[2] The East Australian Current (EAC) (Figure 1) is a component of the western boundary current system of the South Pacific subtropical gyre. The current initially forms near 15°S where the westward flowing South Equatorial Current bifurcates on the Australian coast [Ridgway and Dunn, 2003; Ridgway and Godfrey, 1994] and its volume transport grows as the flow proceeds southward reaching some 22 Sv at latitude 30°S [Mata et al., 2000]. Near latitude 32°S the current turns sharply southeastward away from the Australian coast into the Tasman Sea (Figure 1) and the majority of the transport is directed into the eastward flowing Tasman Front with the remainder continuing southward along the Australian coast. Ridgway and Dunn [2003, Figure 7] describe the EAC surface currents as separating into three major branches shown here in Figure 1. The Tasman Front is the central branch, the southern branch is associated with the subtropical convergence, and the northern branch is a weak North Tasman Current. The approximate separation latitude, mean EAC transport, and the existence of the zonal Tasman Front are predicted by

linear Sverdrup dynamics modified by the presence of the island circulation around New Zealand [Godfrey, 1989]. Upon separation from the coast the EAC undergoes a strong retroflexion that leads to vigorous eddy generation and meandering due to nonlinear dynamics [Tilburg et al., 2001]. Indeed, a characteristic of the EAC that distinguishes it from other western boundary regimes [Stammer, 1997] is that mesoscale variability of the transport is so large (rms 30 Sv at 30°S [Mata et al., 2000]) that on occasions a single continuous current cannot be identified [Godfrey et al., 1980].

[3] Regional observations have noted mesoscale periodicity at around 100 days in temperature and ship-drift velocities [Bennett, 1983; Boland, 1979; Walker and Wilkin, 1998] and 130 days in satellite altimetry [Feron, 1995]. Bowen et al. [2005], using 6 years of surface velocity streamfunction data computed by augmenting altimetry with velocities from sequential thermal imagery [Wilkin et al., 2002], distinguished spectral peaks at 115 and 165 days. The periodicity has been ascribed to the frequency at which anticyclones pinch off from the EAC retroflexion [Godfrey et al., 1980; Nilsson and Cresswell, 1981] and the speed at which meanders in the Tasman Front propagate westward and “break” against the coast [Marchesiello and Middleton, 2000; Nilsson and Cresswell, 1981]. These are local generation processes, whereas Cresswell and Legeckis [1986] contend that “geopotential ridges” from north of the EAC

<sup>1</sup>Institute of Marine and Coastal Sciences, Rutgers, The State University of New Jersey, New Brunswick, New Jersey, USA.

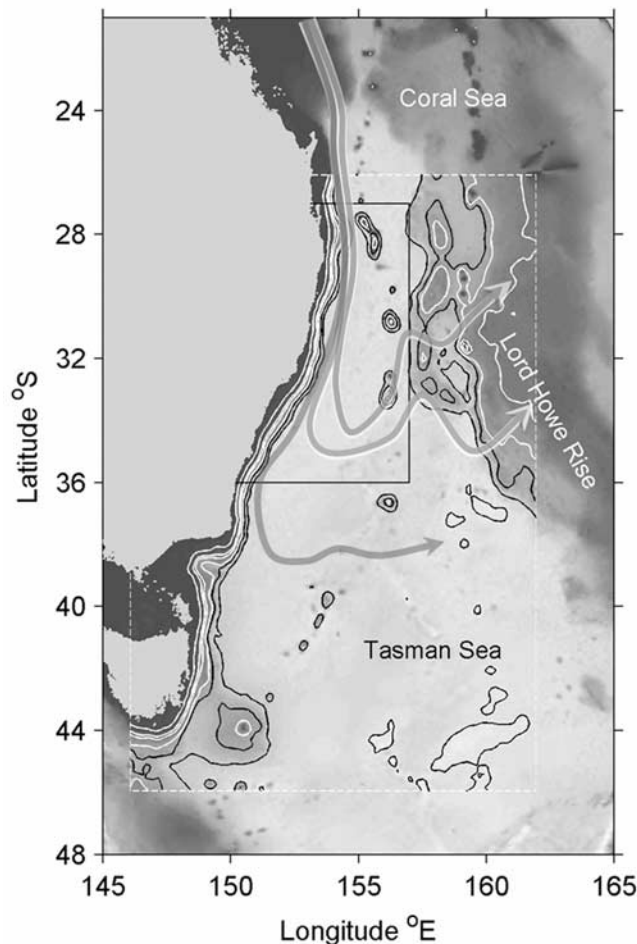


**Figure 1.** Bathymetry of the Tasman Sea (grayscale). White dashed box shows the perimeter of the ROMS model domain. Contours show the model bathymetry (white: 250, 1000, 1500 and 2500 m, black: 3000 and 4000 m). Black box indicates the East Australian Current separation region for which statistical analyses are computed. Arrows depict the schematic of surface currents described by *Ridgway and Dunn* [2003].

propagate toward the south and can significantly affect the eddy formation process. Once formed, the eddies propagate either southwestward into the Tasman Sea or northeastward to coalesce with the main current [*Cresswell and Legeckis*, 1986; *Walker and Wilkin*, 1998].

[4] Whether EAC mesoscale variability is predominantly an intrinsic local instability of the boundary current system or due more to remote forcing was considered by *Bowen et al.* [2005]. They found no evidence that EAC mesoscale variability is coherent with planetary wave activity entering the region from the southwest Pacific east of Lord Howe Rise. Rather, they concluded that westward phase propagation from a region of elevated mesoscale energy immediately to the north and east of the EAC separation was actually the signature of northeastward energy propagation (consistent with short Rossby waves) emanating from a source associated with local instability processes in the separation region. Details of the nature of this instability were not determined.

[5] Modeling studies by *Tilburg et al.* [2001] and *Marchesiello and Middleton* [2000] emphasize the importance of both nonlinear dynamics and local topography in the EAC separation process. In a 70-day simulation, *Marchesiello and Middleton* [2000] showed that Rossby wave dynamics in the propagation of Tasman Front meanders, local acceleration from along-shelf variation in coastal bathymetry, and bottom friction, were all significant in the local depth-averaged vorticity balance in simulations that captured qualitatively the eddy pinch-off process. In this paper we present results from a 5-year simulation of the EAC region using the Regional Ocean Model System (ROMS) that reproduces the equilibrium mesoscale dynamics over many eddy generation, meander, and coalescence events. Validation of the model is by comparison of the mean circulation to the high-resolution CSIRO Atlas of Regional Seas (CARS) [*Ridgway et al.*, 2002] and by comparing complex empirical orthogonal functions (CEOF) of model variability to those observed by *Bowen et al.* [2005]. We also expand upon the CEOF analysis by computing variability in satellite-observed and modeled sea surface temperature (SST). We consider that successfully reproducing the leading order statistical patterns of mesoscale variability is a necessary step prior to using the model for detailed analysis of mesoscale dynamical processes.

[6] The model configuration and simulations are described in the next section, accompanied by an overview of the satellite data sets used in the subsequent analysis. Section 3 describes results from the spectral and CEOF analysis of patterns of mesoscale variability in the model and observations. Section 4 presents a summary of the model-data comparison, and the conclusions regarding regional mesoscale dynamics supported by the combined analysis.

## 2. Model Simulations and Satellite Data

### 2.1. Regional Ocean Model

[7] The numerical simulations were performed with the Regional Ocean Modeling System (ROMS; <http://www.myroms.org>), a model in widespread use for applications from the basin to coastal and estuarine scales [e.g., *Dinniman et al.*, 2003; *Haidvogel et al.*, 2000; *Lutjeharms et al.*, 2003; *MacCready and Geyer*, 2001; *Marchesiello et al.*, 2003; *Peliz et al.*, 2003]. *Shchepetkin and McWilliams* [1998, 2003, 2005] describe in detail the algorithms that comprise the ROMS computational kernel. This kernel utilizes consistent temporal averaging of the barotropic mode to guarantee both exact conservation and constancy preservation properties for tracers and yields more accurate resolved barotropic processes, while preventing aliasing of unresolved barotropic signals into the slow baroclinic motions. Accuracy of the mode-splitting is further enhanced due to redefined barotropic pressure-gradient terms to account for the local variations in density field (i.e., the pressure-gradient truncation error that has previously plagued terrain-following coordinate models is greatly reduced) without sacrificing the efficiency of the split-explicit formulation. Vertical interpolation is performed using a centered fourth-order scheme.

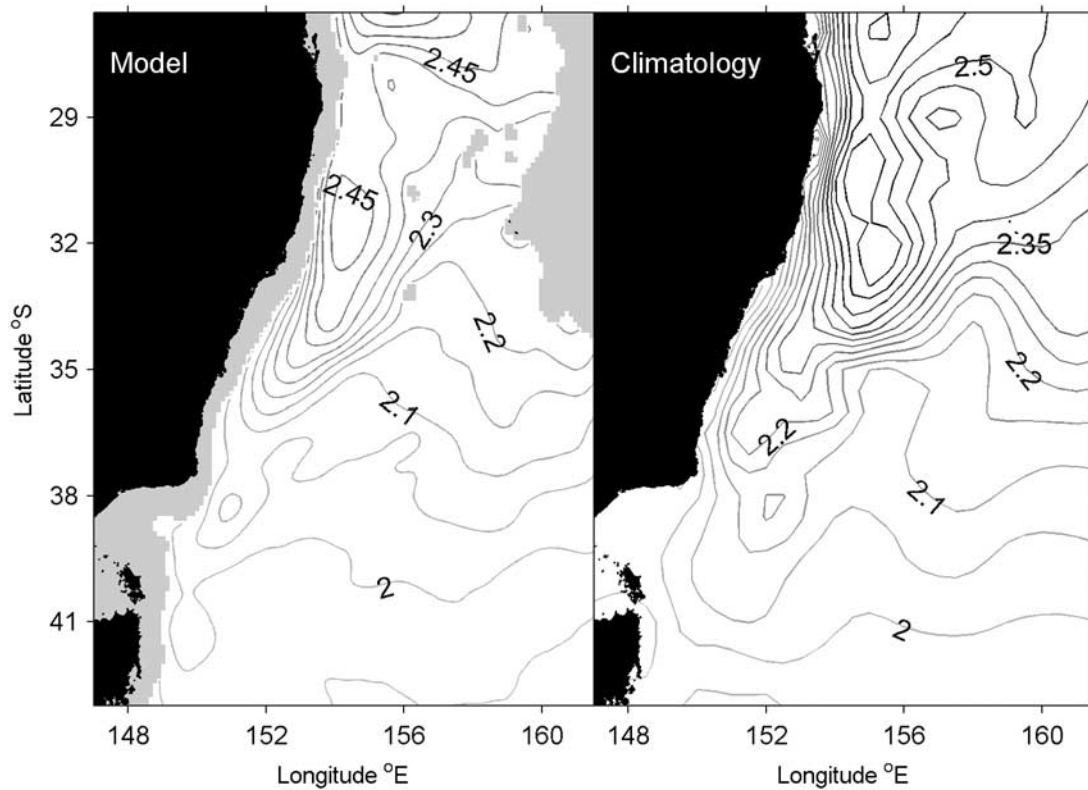


**Figure 2.** Annual mean surface dynamic height (meters) relative to 2000 db. (left) ROMS. (right) CARS climatology [Ridgway *et al.*, 2002]. Regions where depth is shallower than 2000 m are shaded in the model, while for CARS values are based on interpolation of neighboring data.

[8] The model domain spans the region from the Australian coast to 162°E, and 26°S to 46°S (Figure 1). The horizontal grid resolution is 1/8° equal angle (on average 12 km) and there are 30 vertical levels in terrain-following  $s$ -coordinates, weighted toward the surface. The model bathymetry was interpolated from 1/10° equal angle gridded data provided by Geoscience Australia and smoothed with a 24 km scale Gaussian filter. The model open boundary temperature, salinity, and velocity shear were clamped to time series constructed from the annual and semiannual period harmonics of the CARS climatology [Ridgway *et al.*, 2002] with velocities and surface height being computed assuming geostrophy relative to 2000 db. Sea level and depth-integrated velocity open boundary conditions were set using a surface gravity wave radiation scheme [Flather, 1976]. Air-sea heat and momentum fluxes were computed using standard bulk formulae [Fairall *et al.*, 1996] applied to model sea surface temperature and prescribed winds, air temperature, pressure, and humidity from daily averaged U.S. Navy NOGAPS analyses [Rosmond, 1992]. Vertical turbulent mixing closure is by the  $k$ -profile parameterization scheme [Large *et al.*, 1994]. The model was initialized with CARS climatology for 1 January and run for 5 years.

[9] Two years (2001–2002) of NOGAPS daily meteorological data were simply looped to provide continuous surface forcing for the duration of the simulation. We examined meteorological reanalysis data in the region for 1979 through 2005 from the National Centers for Environmental Prediction and found that the 2001–2002 values

were within the expected variance about the long term mean, so we consider the surface forcing used was representative of typical conditions. Ekman pumping from wind stress curl in the Tasman Sea south of 25°S is substantially weaker than further north at 15°S, and it has been shown that patterns in wind driven pumping do not match sea level variability near the coast south of 25°S [Ridgway and Godfrey, 1997], thus local wind forcing itself is not a strong driver of mesoscale dynamics in the EAC separation.

[10] Clamping the regional model open boundary conditions to climatological density and geostrophic velocity successfully produced stable integrations without any conspicuous open boundary artifacts. The annual mean surface dynamic height relative to 2000 m for model and climatology are compared in Figure 2, showing that the dominant features of the regional circulation are reproduced in the interior of the model domain. The local maximum in the recirculation area and the offshore position of the geopotential ridge that defines the retroflexion are captured well. Ridgway and Dunn [2003] find that dynamic heights in the range 2.1 to 2.2 m define the Tasman Front and the model places these contours at the correct latitude in the east of the domain. Quantitative agreement in the southward extent of the retroflexion is less definitive but the pattern is largely correct. Ridgway and Dunn [2003] estimate error bars of  $\pm 0.025$  m for their dynamic height in this region. The climatological maximum geostrophic velocity along the 1500 m isobath [Ridgway and Dunn, 2003, their Figure 12] as a function of latitude is compared with the



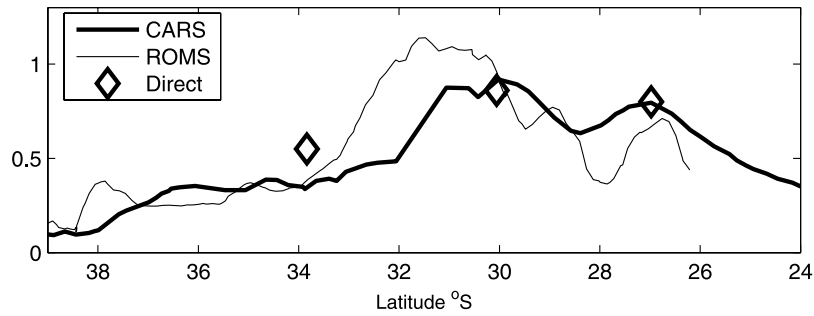


**Figure 3.** Maximum poleward velocity along the 1500 m isobath following the east Australian coast. This is effectively the maximum current within the EAC. Light line indicates ROMS. Heavy line indicates climatological mean geostrophic current [Ridgway and Dunn, 2003]. Symbols denote estimates from current meters and repeat XBT sections.

modeled maximum current in Figure 3. The model captures the accelerating alongshore velocity of the EAC as it approaches the mean separation latitude, and also the occurrence of a local minimum in velocity near 28°S. However, the peak velocity in the model is 20% higher than observed, and the latitude where the poleward current weakens is some 150 km further south. This overly ener-

getic peak velocity is also evident in a complimentary view of the long-term mean velocity shown in Figure 4, which compares zonal sections of modeled meridional velocity within the EAC with observations from the WOCE (World Ocean Circulation Experiment) PCM3 current meter array and repeat hydrography at 30°S [Mata *et al.*, 2000]. The across-shelf extent of the EAC core (southward velocity

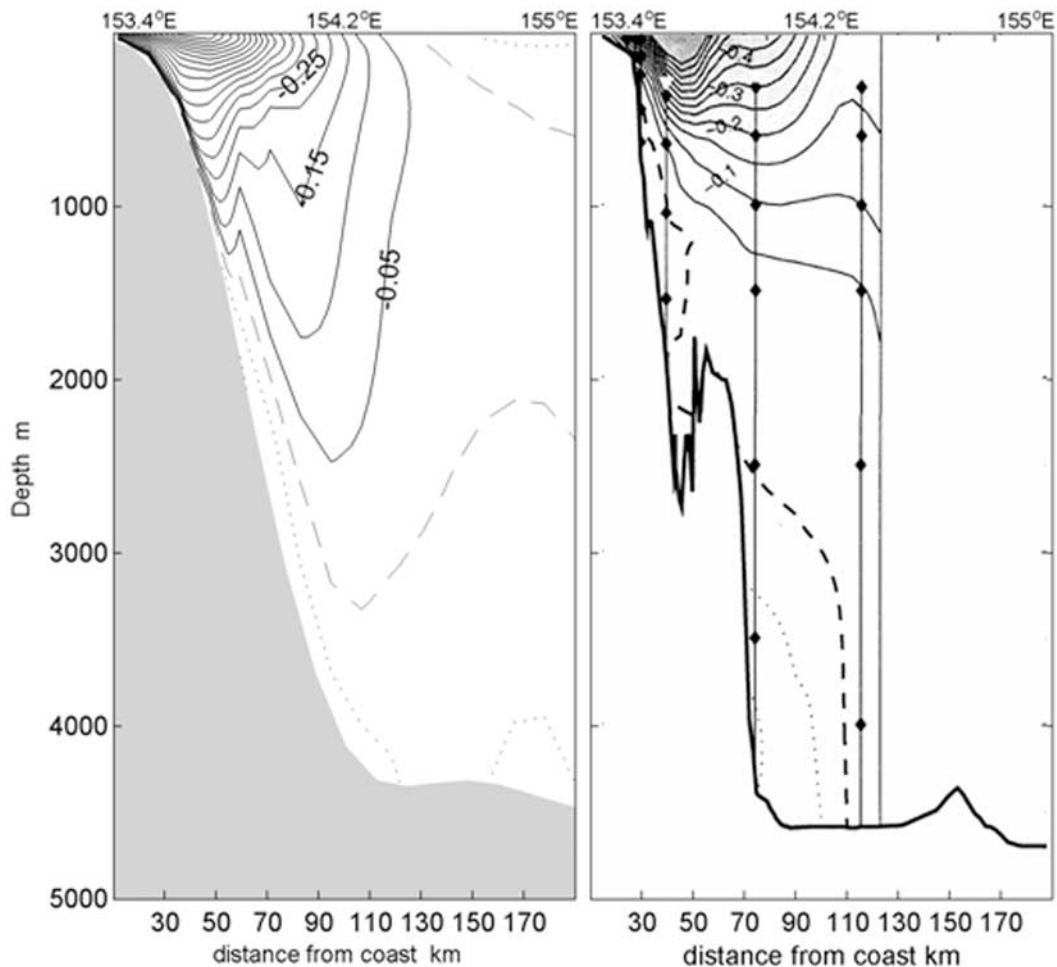


**Figure 4.** Mean meridional velocity in the EAC at 30°S. (left) ROMS annual mean. (right) Observed from current meters and repeat hydrography, reproduced from Mata *et al.* [2000, Figure 5].

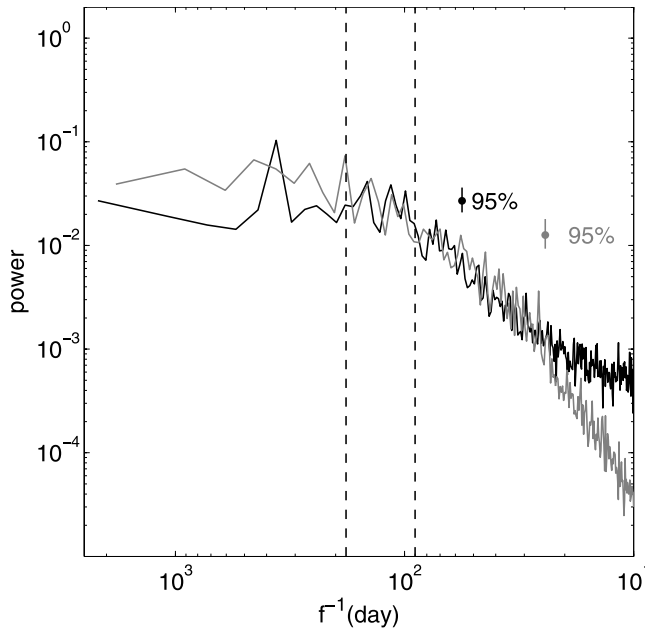


**Figure 5.** Power spectrum of model (grey) and observed (black) streamfunction in the box outlined in Figure 1. Dashed vertical lines indicate the mesoscale band between 180 and 90 days period. Spectra computed at grid points separated by more than  $1^\circ$  longitude and latitude are assumed independent and averaged to calculate the smoothed spectral estimate and the degrees of freedom for the confidence limit indicated. The confidence limit applies to data within the mesoscale band only.

greater than  $0.2 \text{ m s}^{-1}$ ) is correct but the offshore penetration of weaker flow ( $0.05$  to  $0.15 \text{ m s}^{-1}$ ) is absent in the model. The modeled inner shelf currents penetrate down-slope much deeper than observed which is consistent with the model EAC being too fast at this latitude (Figure 3). Both model and observations show a northward subsurface countercurrent against the continental slope.

[11] The comparisons above indicate the model captures the dominant characteristics of the mean circulation observed from hydrography and long-term current-meter mooring deployments. Next we turn our attention to observed and modeled mesoscale variability.

## 2.2. Satellite Sea Surface Temperature and Surface Velocity Streamfunction

[12] A 9-km spatial and 10-day interval surface temperature analysis for the Indo-Australian region was produced by Walker and Wilkin [1998] from daily “best SST” estimates from the NASA/NOAA Pathfinder Program reanalysis of AVHRR (Advanced Very High Resolution Radiometer) observations [Smith et al., 1996]. By fitting spatially varying data covariance functions to local estimates, the optimally interpolated SST analysis retained mesoscale eddy evolution events in the EAC separation region. This 9-year long dataset is well suited to the analysis of mesoscale variability, and we employ a methodology similar to that applied by Bowen et al. [2005] to a comparable resolution dataset of surface velocity streamfunction in the EAC. The streamfunction data were computed by

merging sea surface height anomaly (SSHA) from altimeter satellites with surface velocity estimates obtained from sequential AVHRR image pairs using the method of maximum cross-correlations (MCC) [Bowen et al., 2002]. Multivariate optimal interpolation of these two data sources assumed covariances consistent with two-dimensional geostrophic turbulence [Wilkin et al., 2002] such that the surface velocity streamfunction is related to SSHA through a factor of  $g/f$ , where  $g$  is gravitational acceleration and  $f$  is the local Coriolis parameter. Complex empirical orthogonal functions in the mesoscale frequency band for both these satellite-derived datasets are compared to CEOF patterns from the ROMS simulations in the next section.

## 3. Analysis of Satellite Data and Model Simulations

### 3.1. ROMS Modeled Surface Velocity Streamfunction Variability

[13] To compare with the satellite-derived data, surface geostrophic streamfunction,  $\Psi$ , for ROMS output was estimated as simply the product of  $g/f$  and model SSHA. Though both model SSHA and altimeter data include ageostrophic dynamics, in the analysis that follows frequencies greater than  $1/30$  cycles per day are excluded so SSHA variability can be safely assumed to be predominantly geostrophic. The power spectrum of model  $\Psi$  averaged over the EAC separation region (delineated by the box in Figure 1) is shown in Figure 5. There is a pronounced energy peak at semiannual frequency likely driven by the significant semiannual variability input from the open boundary, while the energy at annual frequency is less conspicuous. Distinct energy peaks in the mesoscale frequency band, which we define as the range from 90 to 180 days period, are statistically significant at the 95% confidence interval. The presence of substantial levels of mesoscale energy in the model output in the absence of boundary forcing in this frequency band suggests the mesoscale variability is generated locally.

[14] The spatial distribution of modeled streamfunction variance in the mesoscale frequency band is shown in Figure 6a. The most intense energy is in the EAC separation region, which further supports the notion the variability is generated locally. Peak values of mesoscale energy follow a band some 200 km off the coast, consistent with the qualitative sense from satellite imagery [Cresswell and Legeckis, 1986; Nilsson and Cresswell, 1981; Walker and Wilkin, 1998] that eddies generated at the typical separation latitude tend to track southwestward parallel to, and constrained by, the coastal boundary. Figure 6b shows the corresponding variance of satellite streamfunction data, and similar elevated energy in a zone parallel to the coast. In the model, there is also the sense of an eastward spread to the mesoscale variability along  $32^\circ\text{S}$ , whereas the observations show this as a more distinct branch to the pattern extending to the southeast. This branching pattern will become more evident in the CEOF analysis that follows.

[15] Figures 5 and 6 shows that the simulated streamfunction variability is more energetic than observed. This may betray a bias toward high eddy variability in the model but could also reflect that while model SSHA variance is calculated at individual grid points, the satellite data were

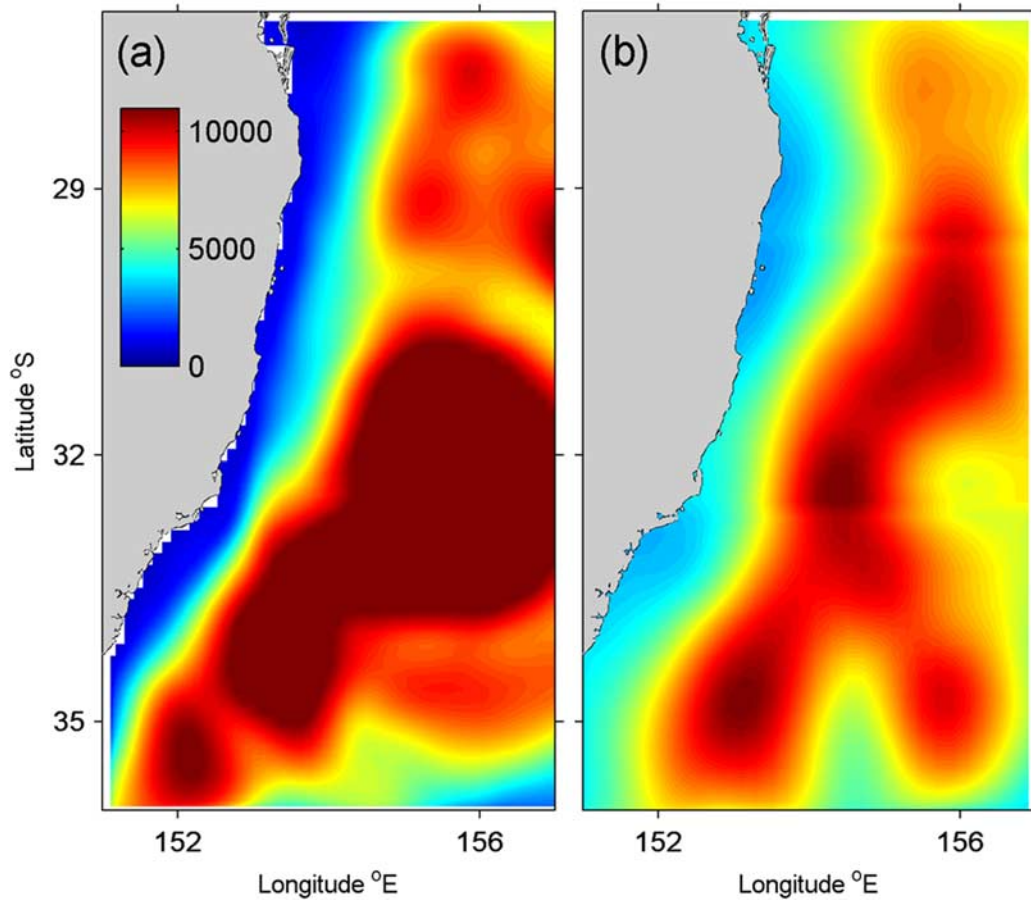


**Figure 6.** Variance of mesoscale frequency band-passed (90 to 180 days period) surface velocity streamfunction,  $\Psi$ , in  $\text{m}^4 \text{s}^{-2}$ . (a) Model. (b) Satellite.

optimally interpolated with a covariance function with a 100 km length scale that acts as a spatial smoother. This diminishes observed peak energy levels. A further difference is that the eastward extension of variance in the model is broader in latitude and centered somewhat north of the southeastward trending ridge of high variance in the observations.

[16] Though the 0/2000 db dynamic height indicates the Tasman Front is at the correct latitude, mean surface currents (Figure 7) show the eastward flow associated with the Tasman Front is located further north in the model than observations. This flow guides eddy variability along a similar trajectory. There is a secondary high variance area in the model at the north of the separation region which has no observed counterpart. This is potentially the result of shortcomings in the open boundary formulation where the EAC enters the domain from the north. Interpretations of the model results must acknowledge that the model solution appears unrealistic in this region.

[17] To seek coherent patterns underlying this mesoscale variability, we apply frequency domain Complex Empirical Orthogonal Function (CEOF) analysis to the model streamfunction to detect propagating wave-like disturbances [Bowen *et al.*, 2005]. The data are first band-pass filtered (90 to 180 day periods) to isolate the mesoscale and avoid unphysical modes entering the results [Merrifield and Guza,

1990], then Hilbert transformed to create complex time series of the data and retain phase information. Empirical Orthogonal Functions (EOF) computed from the covariance of the Hilbert transformed time series return spatial maps of the amplitude and phase of each EOF mode, and time series of their variation [Barnett, 1983; Merrifield and Guza, 1990]. A Monte Carlo method used to compute the criterion for significant eigenvalues of the EOF decomposition [Preisendorfer *et al.*, 1981] (Figure 8) shows that the first two modes (describing 35% and 23% of the variance) are clearly statistically significant, and the third and fourth modes are much less so. The discussion that follows is restricted to modes 1 and 2 only.

[18] Other authors have noted, and we emphasize it here, that EOF interpretation cannot assume the patterns that dominate the statistical variability in observation space will necessarily coincide with the active modes of the underlying dynamical system [Emery and Thompson, 2001]. Nevertheless, in climate dynamics and geophysics this is often a reasonable and useful assumption [von Storch and Zwiers, 1999].

[19] The amplitude and phase of the first two mesoscale CEOF modes of model streamfunction are compared to the patterns calculated by Bowen *et al.* [2005] in Figure 9. The modeled and observed Mode 1 patterns are very similar. Two local maxima in the amplitude occur at comparable

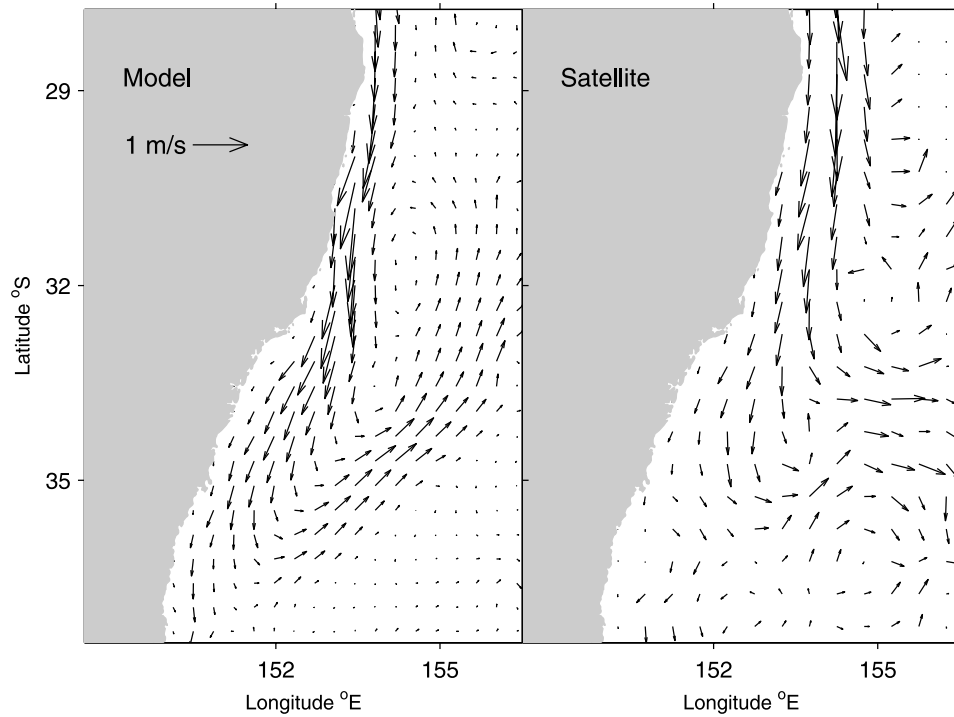


**Figure 7.** Mean surface currents. (left) Model. (right) Satellite.

locations, and both phase patterns show southwestward propagation with a wavelength of about 600 km. We name this the “Eddy Mode” because mesoscale variability propagating along-coast is recognized from qualitative studies as being associated with separated eddies [Cresswell and Legeckis, 1986; Walker and Wilkin, 1998]. The modeled Mode 2 amplitude has a single maximum displaced some

100 km to the north of that observed but both show phase propagation onshore and toward the north in this region. The phase velocity is about  $4 \text{ cm s}^{-1}$  westward, which is comparable to the observed speed of planetary Rossby waves at this latitude [Chelton and Schlax, 1996]. Mode 2 could describe the propagation of some class of Rossby waves, most likely modified by local topography and

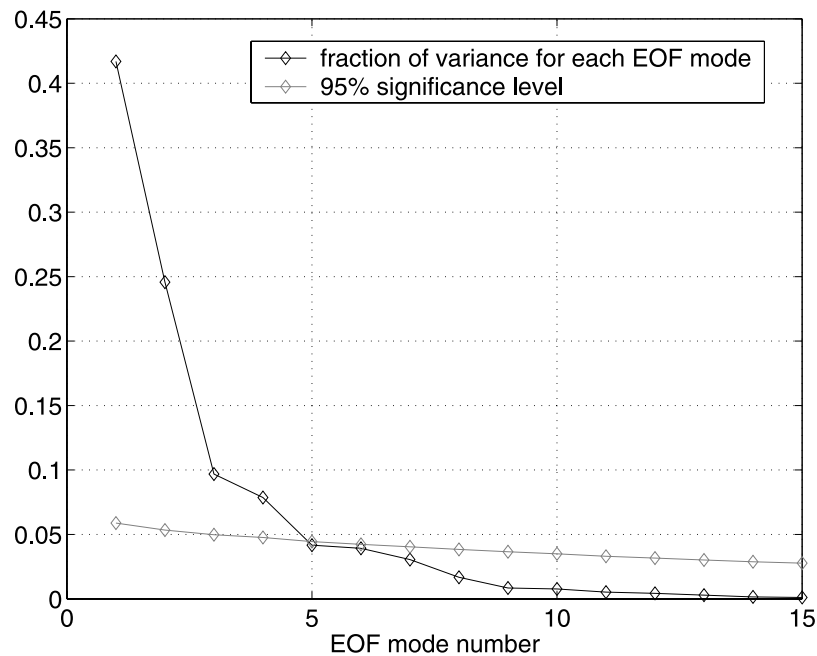


**Figure 8.** Black line indicates a fraction of variance in each Complex Empirical Orthogonal Function mode of the modeled mesoscale streamfunction variability. Grey line indicates 95% significance level from Monte Carlo analysis.



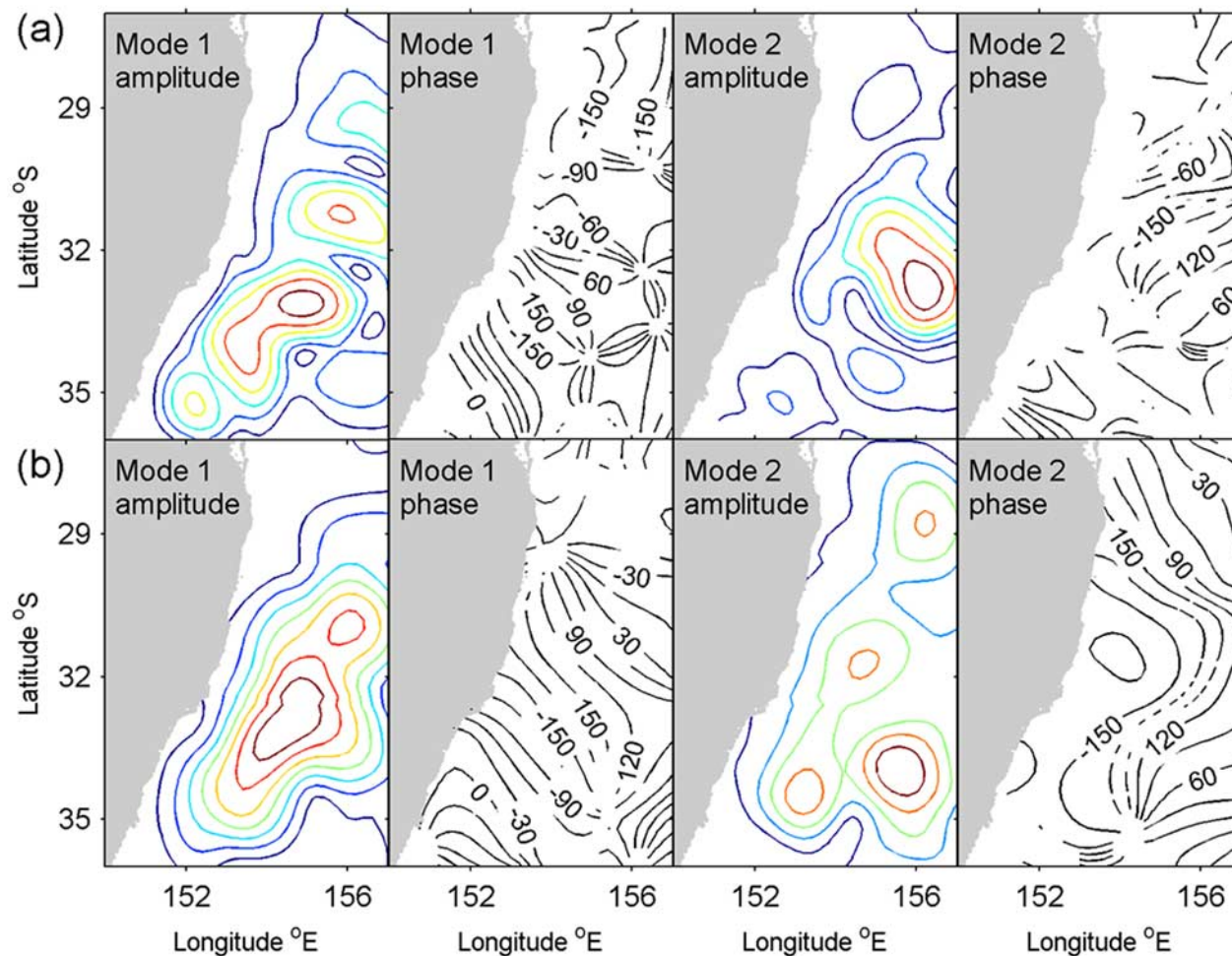


**Figure 9.** Amplitude and phase of CEOF spatial patterns of mesoscale surface velocity streamfunction. (a) Model. (b) Satellite.

background mean circulation, and so we name it the “Wave Mode.” Other, smaller, maxima in the observed Mode 2 amplitude laying along an arc parallel to the coast are absent from the model. In the northeast there is a region of clearly southwestward advancing phase where the observed Mode 2 amplitude is substantially stronger than modeled. This difference between model and data would be consistent with the observed Mode 2 variability having a remote source outside the limits of the model domain; recall that the model open boundary conditions have strictly annual and semiannual harmonic variability with no energy in the mesoscale band. We will return to this issue in the discussion section.

[20] For completeness, the modal amplitude time series are plotted in Figure 10 for comparison with the results of *Bowen et al.* [2005, Figure 9], though it cannot be expected that there be any direct event-wise correspondence in the time series given the climatological open boundary conditions used in the present ROMS configuration.

### 3.2. ROMS Modeled Sea Surface Temperature Variability

[21] Figure 11 shows the power spectrum of ROMS SST computed in the same manner as Figure 5 for  $\Psi$ . The largest energy peak is at annual frequency due to the open

boundary forcing and the strong influence of seasonal heating and cooling on the surface mixed layer temperature. There are spectral peaks significant at the 95% confidence level in the mesoscale band, but they are not as distinct as those in the streamfunction spectrum. Variance of mesoscale band-passed ROMS SST data is shown in Figure 12. The high variance regions are not as compact as the streamfunction variance, but the overall patterns are similar. Variance maxima occur in the southwest where the mean EAC path retroflects and in the southeast where the Tasman Front meanders. There is high SST variance in the same region in the northeast where model streamfunction variance is elevated in contradiction with observations.

[22] The main difference between the patterns of model  $\Psi$  and SST variability is the low SST variance centered on 31°S, 154°E. Surface temperatures in this area are persistently high with low variability due to the steady influx of warm water from the EAC. Between 30°S and 33°S the SST variance is low along the coast in the core of the EAC but moderately higher in a parallel belt some 75 km offshore due to meandering of the edge of the boundary current.

[23] The results of mesoscale CEOF analysis of ROMS SST are plotted in Figures 13 and 14. The amplitude time



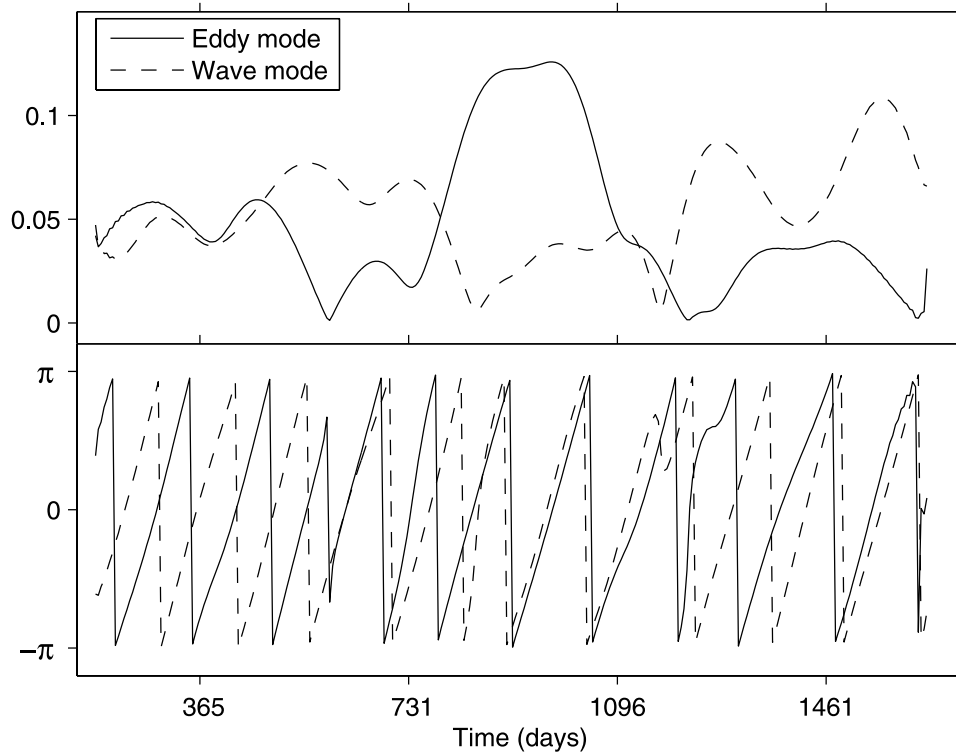


**Figure 10.** (top) Amplitude and (bottom) phase of CEOF time series of modeled mesoscale surface velocity streamfunction. Solid line indicates mode 1. Dashed line indicates mode 2.

series (Figure 14) are similar to those obtained for streamfunction with cross-correlations of 0.92 and 0.52 for modes 1 and 2, respectively. The modes describe similar phenomena. Mode 1 again shows energy propagation along the coast (the Eddy Mode), while Mode 2 shows onshore Rossby wave-like propagation (the Wave Mode).

[24] The Mode 1 amplitude has a ridge parallel to the coast between 30°S and 33°S but is low immediately adjacent to the coastline in the core of EAC, indicating that the migrating eddy pattern has only a moderate projection onto variability in the EAC itself when the current is still attached to the coast. The phase advances southward in this near coastal band, consistent with the observed movement of meanders in the outer edge of the EAC. Mode 1 maxima centered on 33.5°S, 155°E and 35.5°S, 152°E have corresponding peaks in the streamfunction Eddy Mode (Figure 9a).

[25] In contrast to the  $\Psi$  Eddy Mode, the SST pattern has a distinct minimum where the separated EAC front typically lays [Godfrey *et al.*, 1980], yet the Mode 1 phase still advances predominantly toward the southwest in common with the streamfunction Eddy Mode. Mesoscale eddies travel through this region producing oscillations in SSHa and streamfunction, but this does not translate to variability in SST because the surface temperature signal is masked by the influence of warm EAC waters recently separated from the coast. Vertical sections in the region where the boundary current retroflection has strong anticyclonic curvature typically show a relatively thin wedge of warm EAC water at the surface so that the surface thermal front lays to the southwest of the maximum gradient in surface dynamic height. Under such circumstances of strong near surface

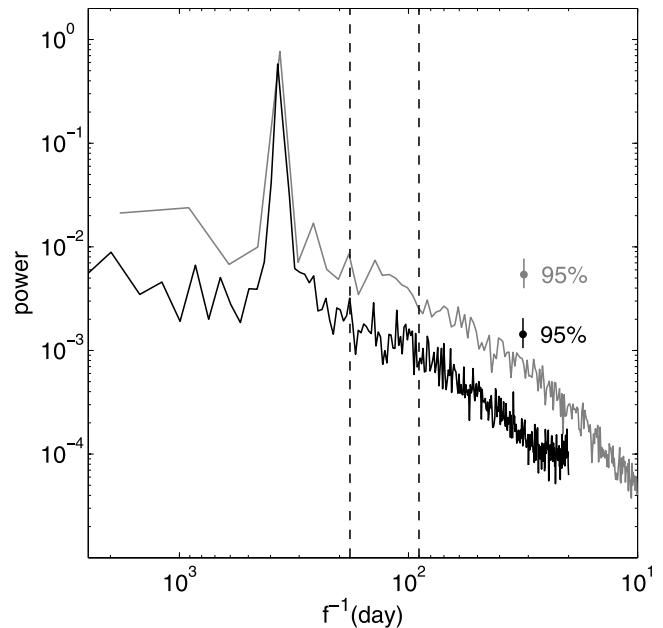


**Figure 11.** Power spectrum of modeled (grey) and observed (black) sea surface temperature variability. Dashed vertical lines indicate the mesoscale band between 180 and 90 days period. Spectra computed at points separated by more than 1° longitude and latitude are assumed independent and averaged to calculate the smoothed spectral estimate and the degrees of freedom for the confidence limit indicated. The confidence limit applies to data within the mesoscale band only.

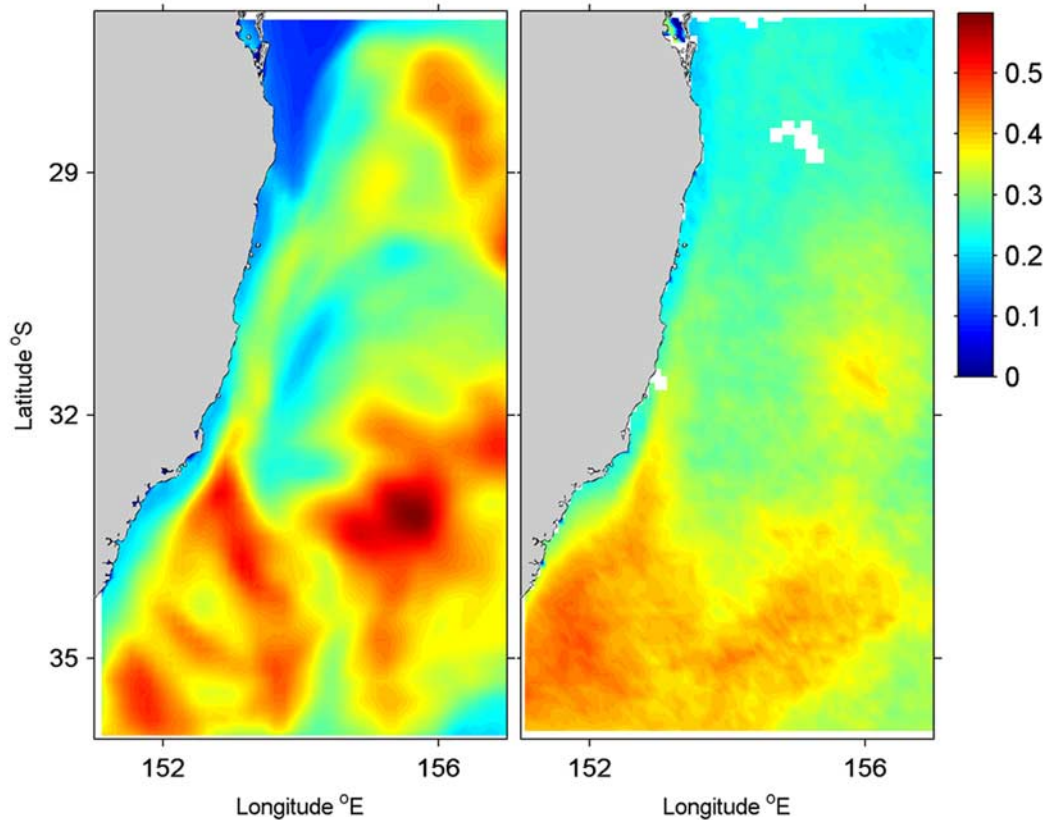


**Figure 12.** Variance of mesoscale frequency band-passed (90 to 180 days period) model sea surface temperature in  $^{\circ}\text{C}^2 \text{ s}^{-2}$ . (left) Model. (right) Satellite.

thermal stratification, variability in SST due to displacements of the surface expression of the temperature front will not have a correspondingly large signature in SSHA and streamfunction.

[26] Examining animations (<http://marine.rutgers.edu/~wilkin/WilkinZhang2006>) of the reconstructed Eddy Mode we observe a zigzag propagation track for the SST variability. Starting near  $30^{\circ}\text{S}$ , perturbations move southward parallel to the coastline, abruptly turn away from the coast at the separation latitude and ride on the mean EAC, and then turn again to the southwest once they have propagated across the Tasman Front. Looking more closely at the Eddy Mode phase this sense to the propagation can also be seen by following a trajectory normal to the phase contours of Figure 13. The same trajectory is evident when following the phase of the  $\Psi$  Eddy Mode (Figure 9).

[27] The model SST Wave Mode has regions of high and low amplitude in close proximity, with many zones of seemingly chaotic phase. However, north of the EAC separation where the amplitude is high there is northwestward on-shore propagation similar to the modeled  $\Psi$  Wave Mode. Where the SST Wave Mode amplitude is significant within and south of the separation region, there are no consistent gradients in phase indicating the variability is more akin to a standing wave in this region. This result is also true of the modeled  $\Psi$  Wave Mode.

[28] The modeled SST Eddy and Wave modes have 28% and 17% of the total mesoscale SST variance, respectively, both of which are lower than those of observed and modeled

mesoscale  $\Psi$  variance. These low eigenvalues and the generally less coherent phase patterns suggest that SST is a less fundamental indicator of mesoscale dynamics than SSHA or surface velocity streamfunction. As a test of this conjecture we performed a CEOF analysis of the model temperature at 250 m depth ( $T_{250}$ ). Charts of  $T_{250}$  derived from expendable bathythermographs (XBT) have been used by the Royal Australian Navy as an indicator of EAC eddy locations since before the advent of satellite altimetry. The CEOFs of  $T_{250}$  (not shown) are almost identical to those from model SSHA. Where SST and streamfunction modes differ this is presumably due to their associated vertical dynamic structures having strong vertical shear above the thermocline that do not project significantly onto subsurface geopotential anomalies.

[29] We tested whether air-sea heat fluxes could be active in driving mesoscale variability in SST. If this were significant, there would be a correlation between the time integral of net heat flux and SST, or equivalently, heat flux and time-rate-of-change of SST. We found no correlation and conclude that the drivers of mesoscale variability are in the circulation.

### 3.3. Satellite-Observed Sea Surface Temperature Variability

[30] The power spectrum of satellite observed SST variability (Figure 11) shows a clear peak at annual frequency, and peaks within the mesoscale frequency band that are significant at the 95% confidence level. The map of

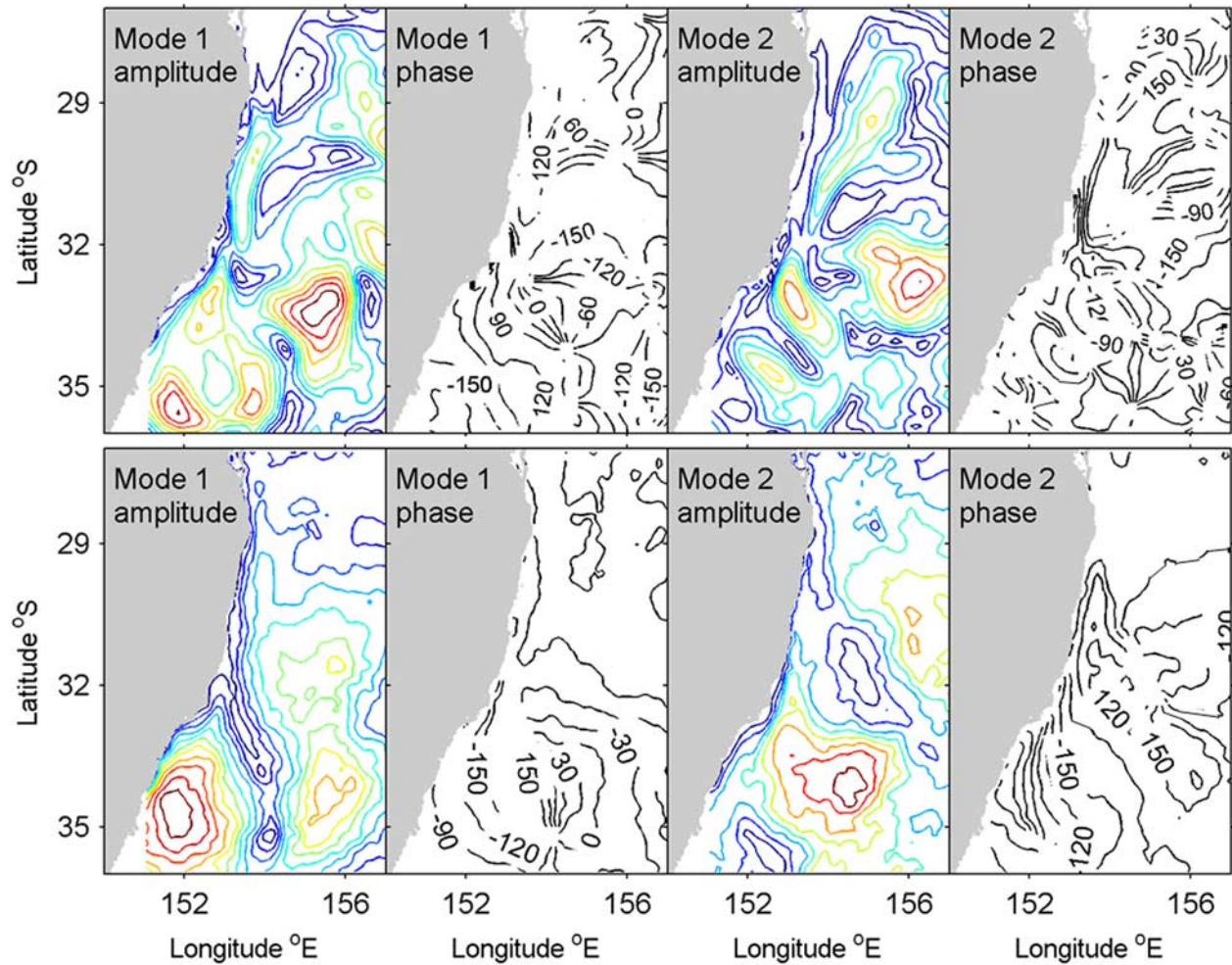


**Figure 13.** Amplitude and phase of CEOF spatial patterns of mesoscale sea surface temperature. (top) Model. (bottom) Observed pattern after Varimax rotation.

observed mesoscale SST variance (Figure 12) exhibits patterns similar to those of the model SST with the exception of the unrealistically high amplitude in the north that was noted previously in the comparison of observed and modeled streamfunction variability. As was the case for streamfunction, the maximum observed SST variance is less than modeled. Evidently, the model somewhat overestimates the mesoscale fluctuations of both SSHA and SST.

[31] The mesoscale band-passed SST data were again Hilbert transformed and factored into CEOFs. The results were found to depend on the extent of the spatial subset selected for the CEOF calculation. Such subdomain instability is a common problem with EOF analysis and can be largely eliminated by a suitably chosen rotation of the eigenvectors [Mestas-Nunez, 2000; Richman, 1986]. Applying the orthogonal rotations of the Varimax method [Richman, 1986] eliminates the subdomain dependence of these data; the resulting patterns are shown in Figure 13. Mode 1 contains 21% of the total variability, while the second mode contains 18%. Mode 1 has greatest amplitude southwest of the mean EAC front where the modeled Mode 1 is also large, though the modeled mode is fragmented into three local maxima. A second maximum in Mode 1 at 34.5°S,

155.5°E lies where the Tasman Front oscillates over a large latitude range. Mode 1 is weak in a band following the course of the separated EAC echoing the pattern seen in the modeled SST Eddy Mode. Phase contours, too, are similar, showing southward propagation across the EAC front that then turns southwestward confirming that the zigzag trajectory of SST anomalies associated with Mode 1 in the ROMS model are correctly simulated.

[32] In contrast, the Mode 2 amplitude could be interpreted as emanating from the EAC separation point near Sugarloaf Point at 32°S and building to a maximum at 34°S, 154.5°E. While the model Mode 2 is similar at the coast, it takes a clearly distinct local maximum northeast of the observed maximum (Figure 13). Arguably, there is coherent westward phase propagation connecting the two maximum in the modeled SST Mode 2 but this pattern is much less consistent, as was the case in the comparison of modeled and observed phase of the streamfunction Mode 2.

#### 4. Discussion and Conclusions

[33] The regional ocean model configuration adopted here uses climatology data to specify initial and open



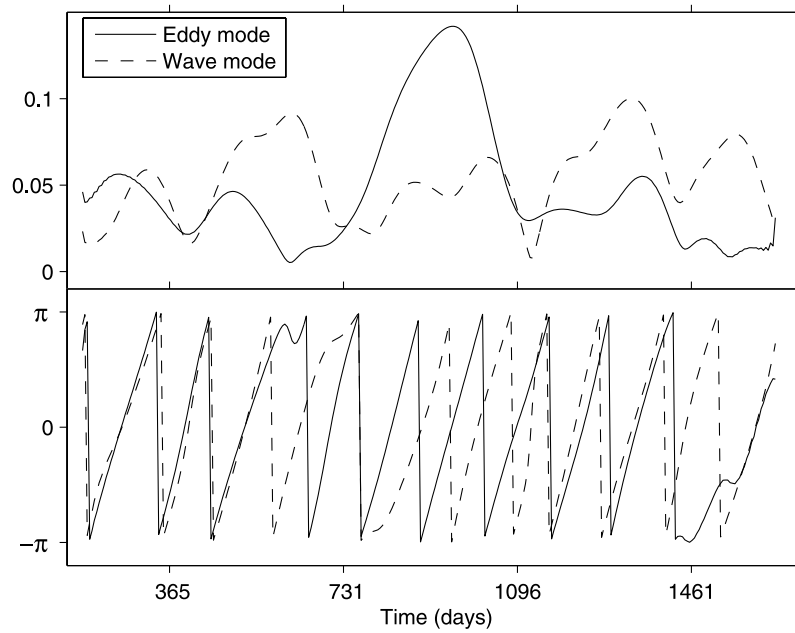


**Figure 14.** (top) Amplitude and (bottom) phase of CEOF time series of modeled sea surface temperature. Solid line indicates Mode 1. Dashed line indicates Mode 2.

boundary conditions for a 5-year simulation. It is therefore not possible to compare model time series directly to observed time series as a check of the accuracy of the simulation. In lieu of such a comparison, our approach has been to verify that both the mean model circulation and, more importantly, detailed statistical descriptions of its mesoscale variability compare favorably to long-term satellite observations. Since the early idealized study of *Godfrey* [1973], EAC models have been able to qualitatively simulate eddy formation events, yet the principal dynamical processes responsible remain a source of speculation. Recent high-resolution studies by *Marchesiello and Middleton* [2000] and *Tilburg et al.* [2001] emphasize the role of nonlinear dynamics but the relative importance of barotropic versus baroclinic instability is unspecified. Prior to any analysis of eddy energetics it should be established that a model captures the leading order statistical patterns of mesoscale variability in order to have some confidence that the model generates eddy variability for the correct dynamical reasons. This is the motivation for our close scrutiny of CEOFs of modeled and observed mesoscale surface temperature and velocity variability.

[34] We have shown that model and data energy spectra both have peaks in the mesoscale band (90 to 180 days period), and Complex EOF analysis factors this variability into two statistically significant modes. Mode 1 we refer to as the Eddy Mode because reconstructions of the mode time series resemble the character of the evolution of EAC eddies long recognized from observational studies. Surface temperature anomalies originate near 30°S and follow a zigzag path first southward, then swept eastward by the EAC where it is newly separated from the coast, and subsequently southwestward again once the anomaly has crossed the Tasman Front.

[35] The correspondence is strong between the modeled and observed Eddy Mode in the surface velocity stream-

function. The overall spatial pattern and the direction and speed of phase propagation within and to the south of the EAC separation region agree well. The modeled and observed Eddy Modes in SST also have points of agreement, notably a pronounced minimum along the axis of EAC jet and southwestward phase propagation similar to that of streamfunction. Since the modeled patterns of the dominant EOF of eddy variability in the separation region concur with those observed by satellite, we take this as a strong indication that the model correctly reproduces the dynamical mechanisms of mesoscale instability in this boundary current system. No mesoscale frequencies are imposed externally through the open boundary conditions, leading us to conclude that the eddy variability is generated locally through an intrinsic instability of the flow.

[36] However, while Mode 1 agrees well within the separation region, a modeled high variance region occurs in the north without an observed counterpart. We do not have an explanation for this, but it may indicate a deficiency in the manner in which the open boundary conditions are applied (by clamping) or how boundary velocities are specified (i.e., geostrophy relative to a fixed reference depth) near the steep and shallow bathymetry of the Lord Howe Rise in the northeast corner of the model domain.

[37] Mode 2 (or the Wave Mode) in observed streamfunction has southwestward phase propagation in the north of the domain and northwestward propagation in the south. For short Rossby waves this implies group velocity and hence energy propagation [*Hendershott*, 1981] emanating from the EAC separation region, which *Bowen et al.* [2005] note is consistent with a local source for this mode also. Furthermore, their wavelet analysis of altimeter SSHA (designed to isolate mesoscale frequency wave trains) found no evidence of mesoscale energy entering the EAC region from the southwest Pacific Ocean, discounting the suggestion advanced in other studies that wave-like disturbances

might enter from the north and east. The modeled Wave Mode shows the northwestward phase propagation for both  $\Psi$  and SST in the center and south of the analysis region, but no trace of the southwestward phase propagation branch in the north that is so clear in the observed  $\Psi$ . The model results are therefore ambiguous in their support of the notion that the Wave Mode is generated locally.

[38] A possible explanation for Mode 2 not considered by Bowen *et al.* [2005] is a nearby source such as the passage of planetary waves over a mid-ocean ridge [Barnier, 1988; Moore and Wilkin, 1998], namely the Lord Howe Rise, or topographic waves along the ridge itself that could radiate energy westward. In the present model the lack of mesoscale frequency boundary forcing again argues against the former mechanism, but the interaction of mesoscale variability of the Tasman Front with the Lord Howe Rise near the eastern limit of the model domain could admit the latter mechanism. These are speculative conclusions that would require a larger domain model and further analysis to resolve.

[39] EOFs form a complete basis set, so dynamical equations can be projected efficiently onto a truncated set of dominant EOFs in a spectral model, an approach that has been used to formulate simple spectral models of the atmosphere and ocean [Roulston and Neelin, 2003; Selten, 1995]. Though the EOFs are orthogonal they do not evolve independently because nonlinearities in the model dynamics couple the modes over a finite time interval. However, Selten [1995] found that linear damping of each individual mode was a successful closure for unresolved scales, more so than for conventional spectral modes based on spherical harmonics, and he concluded that the coupling of the modes was relatively weak. This was ascribed, in part, to some nonlinearity in the response being embodied in the EOF patterns themselves, but also for the reason that EOFs select dominant coherent circulation structures and this tends to separate fast and slow structures that do not appreciably interact.

[40] We mention these results because they are pertinent to the issue of whether the eddy variability is related to wave dynamics in the EAC region. The Wave and Eddy Modes are statistically uncorrelated (because they are orthogonal) but, as noted above, variability with these patterns would become correlated in a nonlinear ocean, though any such coupling might be expected to be weak. We are unable to determine unambiguously whether the source of the Wave Mode energy is within or outside the EAC separation (though it is not beyond the limits of the model domain), so it seems prudent to conclude that we have no evidence or strong reasons to suspect that the Wave Mode plays a role in the EAC eddy formation process.

[41] Though the time series of modeled Mode 1 streamfunction and SST are strongly correlated, their spatial patterns differ. Streamfunction shows consistent southwestward phase propagation across the EAC front, whereas SST takes the zigzag path discussed above where the SST Mode 1 amplitude is low. We have ascribed these differences to the strong thermal signal of the separated EAC obscuring SST variability, and substantial vertical gradients in the upper 250 m of the water column because the  $T_{250}$  Eddy Mode resembles that of surface streamfunction. Bowen *et al.* [2005], echoing the conjecture of Stammer

[1997], present evidence that barotropic instability could be responsible for the Eddy Mode variability. However, if this were so then we might expect the mesoscale SST and  $T_{250}$  variability to be more synchronized.

[42] In summary:

[43] 1. Formulating a model of the EAC region using open boundary conditions specified from annual and semi-annual harmonic climatological tracer variability, and geostrophy, admits a realistic simulation of the mean circulation and mesoscale eddy variability. Characterized in terms of Complex EOFs, the variability agrees well with modes computed from long time series of satellite SST and surface velocity.

[44] 2. In particular, the amplitude and phase propagation characteristics of the mesoscale Eddy Mode in model and data agree closely, indicating that the dynamical processes and scales that lead to the eddy variability are simulated well.

[45] 3. Eddy variability in the EAC is not remotely forced, but generated locally through intrinsic instability of the flow. The relative importance of barotropic and baroclinic instabilities remains undetermined, but there is evidence for both processes being active. Since the model reproduces satellite-observed statistical patterns of mesoscale variability, analysis of the model energetics from the multiyear simulation has the potential to quantify the relative importance of barotropic and baroclinic instability processes.

[46] **Acknowledgments.** This work was funded by Office of Naval Research grant N00014-03-1-0227. ROMS model development is funded by ONR. Computational resources were provided by the DOD High Performance Computing Modernization Program. We thank R. Preller and P. Posey of the Naval Research Laboratory for providing the NOGAPS forcing data and M. Mata for permission to present the EAC mooring data.

## References

- Barnett, T. P. (1983), Interaction of the monsoon and Pacific trade wind system at interannual time scales. part I: The equatorial zone, *Mon. Weather Rev.*, **111**, 756–773.
- Barnier, B. (1988), A numerical study on the influence of the Mid-Atlantic Ridge on nonlinear first-mode baroclinic Rossby waves generated by seasonal winds, *J. Phys. Oceanogr.*, **18**, 417–433.
- Bennett, A. F. (1983), The South Pacific including the East Australian Current, in *Eddies in Marine Science*, edited by A. Robinson, pp. 219–244, Springer, New York.
- Boland, F. M. (1979), A time series of expendable bathythermograph (XBT) sections across the East Australian Current, *Aust. J. Mar. Freshwater Res.*, **30**, 303–313.
- Bowen, M. M., W. J. Emery, J. L. Wilkin, P. Tildesley, I. Barton, and R. Knewton (2002), Extracting multi-year surface currents from sequential thermal imagery using the Maximum Cross Correlation technique, *J. Atmos. Oceanic Technol.*, **19**, 1665–1676.
- Bowen, M. M., J. L. Wilkin, and W. J. Emery (2005), Variability and forcing of the East Australian Current, *J. Geophys. Res.*, **110**, C03019, doi:10.1029/2004JC002533.
- Chelton, D. B., and M. G. Schlax (1996), Global observations of oceanic Rossby waves, *Science*, **272**, 234–238.
- Cresswell, G. R., and R. Legeckis (1986), Eddies off southeastern Australia, *Deep Sea Res., Part A*, **33**, 1527–1562.
- Dinniman, M. S., J. M. Klinck, and W. O. Smith Jr. (2003), Cross-shelf exchange in a model of the Ross Sea circulation and biogeochemistry, *Deep Sea Res., Part II*, **50**, 3103–3120.
- Emery, W. J., and R. E. Thompson (2001), *Data Analysis Methods in Physical Oceanography*, 2nd ed., 638 pp., Elsevier, New York.
- Fairall, C., E. Bradley, D. Rogers, J. Edson, and G. Young (1996), Bulk parameterization of air-sea fluxes for TOGA COARE, *J. Geophys. Res.*, **101**, 3747–3764.
- Feron, R. C. V. (1995), The Southern Ocean western boundary currents: Comparison of fine resolution Antarctic model results with Geosat altimeter records, *J. Geophys. Res.*, **100**, 4959–4975.

- Flather, R. A. (1976), A tidal model of the northwest European continental shelf, *Mem. Soc. R. Sci. Liege, Ser. 6*, 10, 141–164.
- Godfrey, J. S. (1973), Comparison of the East Australian Current with the western boundary flow in Bryan and Cox's (1968) numerical model ocean, *Deep Sea Res.*, 20, 1059–1076.
- Godfrey, J. S. (1989), A Sverdrup model of the depth-integrated flow for the World Ocean allowing for island circulations, *Geophys. Astrophys. Fluid Dyn.*, 45, 89–112.
- Godfrey, J. S., G. R. Cresswell, T. J. Golding, A. F. Pearce, and R. Boyd (1980), The separation of the East Australian Current, *J. Phys. Oceanogr.*, 10, 430–440.
- Haidvogel, D. B., H. G. Arango, K. S. Hedström, A. Beckmann, P. Malanotte-Rizzoli, and A. F. Shchepetkin (2000), Model evaluation experiments in the North Atlantic Basin: Simulations in nonlinear terrain-following coordinates, *Dyn. Atmos. Oceans*, 32, 239–281.
- Hendershott, M. (1981), Long waves and ocean tides, in *Evolution of Physical Oceanography*, edited by B. Warren and C. Wunsch, pp. 292–341, MIT Press, Cambridge, Mass.
- Large, W. G., J. C. McWilliams, and S. C. Doney (1994), Oceanic vertical mixing: A review and a model with a nonlocal boundary layer parameterization, *Rev. Geophys.*, 32, 363–403.
- Lutjeharms, J. R. E., P. Penven, and C. Roy (2003), Modelling the shear edge eddies of the southern Agulhas Current, *Cont. Shelf Res.*, 23, 1099–1115.
- MacCready, P., and W. R. Geyer (2001), Estuarine salt flux through an isohaline surface, *J. Geophys. Res.*, 106, 11,629–11,637.
- Marchesiello, P., and J. H. Middleton (2000), Modeling the East Australian Current in the western Tasman Sea, *J. Phys. Oceanogr.*, 30, 2956–2971.
- Marchesiello, P., J. C. McWilliams, and A. F. Shchepetkin (2003), Equilibrium structure and dynamics of the California Current System, *J. Phys. Oceanogr.*, 33, 753–783.
- Mata, M. M., M. Tomczak, S. Wijffels, and J. Church (2000), East Australian Current volume transports at 30°S: Estimates from the World Ocean Circulation Experiment hydrographic sections PR11/P6 and the PCM3 current meter array, *J. Geophys. Res.*, 105, 28,509–28,526.
- Merrifield, M. A., and R. T. Guza (1990), Detecting propagating signals with complex empirical orthogonal functions: A cautionary note, *J. Phys. Oceanogr.*, 20, 1628–1633.
- Mestas-Nunez, M. A. (2000), Orthogonality properties of rotated empirical modes, *Int. J. Climatol.*, 20, 1509–1516.
- Moore, M. I., and J. L. Wilkin (1998), Variability in the South Pacific Deep Western Boundary Current from current meter observations and a high-resolution global model, *J. Geophys. Res.*, 103, 5439–5457.
- Nilsson, C. S., and G. R. Cresswell (1981), The formation and evolution of East Australian Current warm core eddies, *Prog. Oceanogr.*, 9, 133–183.
- Peliz, A., J. Dubert, D. B. Haidvogel, and B. Le Cann (2003), Generation and unstable evolution of a density-driven Eastern Poleward Current: The Iberian Poleward Current, *J. Geophys. Res.*, 108(C8), 3268, doi:10.1029/2002JC001443.
- Preisendorfer, R. W., F. W. Zwiers, and T. P. Barnett (1981), Foundations of principal component selection rules, *SIO Ref. Ser. 81-4*, 192 pp., Scripps Inst. of Oceanogr., La Jolla, Calif.
- Richman, M. B. (1986), Rotation of principal components, *J. Climatol.*, 6, 293–335.
- Ridgway, K. R., and J. R. Dunn (2003), Mesoscale structure of the mean East Australian Current System and its relationship with topography, *Prog. Oceanogr.*, 56, 189–222.
- Ridgway, K. R., and J. S. Godfrey (1994), Mass and heat budgets in the East Australian Current: A direct approach, *J. Geophys. Res.*, 99, 3231–3248.
- Ridgway, K. R., and J. S. Godfrey (1997), Seasonal cycle of the East Australian Current, *J. Geophys. Res.*, 102, 22,921–22,936.
- Ridgway, K. R., J. R. Dunn, and J. L. Wilkin (2002), Ocean interpolation by 4-dimensional weighted least squares: Application to the waters around Australasia, *J. Atmos. Oceanic Technol.*, 19, 1357–1375.
- Rosmond, T. E. (1992), The design and testing of the Navy Operational Global Atmospheric Prediction System, *Weather Forecasting*, 7, 262–272.
- Roulston, M. S., and J. D. Neelin (2003), Non-linear coupling between modes in a low-dimensional model of ENSO, *Atmos. Ocean*, 41, 217–231.
- Selten, F. (1995), An efficient description of the dynamics of barotropic flow, *J. Atmos. Sci.*, 52, 915–936.
- Shchepetkin, A. F., and J. C. McWilliams (1998), Quasi-monotone advection schemes based on explicit locally adaptive diffusion, *Mon. Weather Rev.*, 126, 1541–1580.
- Shchepetkin, A. F., and J. C. McWilliams (2003), A method for computing horizontal pressure-gradient force in an oceanic model with a nonaligned vertical coordinate, *J. Geophys. Res.*, 108(C3), 3090, doi:10.1029/2001JC001047.
- Shchepetkin, A. F., and J. C. McWilliams (2005), The regional oceanic modeling system (ROMS): A split-explicit, free-surface, topography-following-coordinate oceanic model, *Ocean Modell.*, 9, 347–404.
- Smith, E., J. Vazquez, A. Tran, and R. Sumagaysay (1996), *Satellite-Derived Sea Surface Temperature Data Available From the NOAA/NASA Pathfinder Program*, [http://www.agu.org/eos\\_elec/95274e.html](http://www.agu.org/eos_elec/95274e.html), AGU, Washington, D. C.
- Stammer, D. (1997), Global characteristics of ocean variability estimated from regional TOPEX/Poseidon altimeter measurements, *J. Phys. Oceanogr.*, 27, 1743–1769.
- Tilburg, E. C., H. E. Hurlbert, J. J. O'Brien, and J. F. Shriver (2001), The dynamics of the East Australian Current system: The Tasman Front, the East Auckland Current, and the East Cape Current, *J. Phys. Oceanogr.*, 31, 2917–2943.
- von Storch, H., and F. W. Zwiers (1999), *Statistical Analysis in Climate Research*, 494 pp., Cambridge Univ. Press, New York.
- Walker, A. E., and J. L. Wilkin (1998), Optimal averaging of NOAA/NASA Pathfinder satellite sea surface temperature data, *J. Geophys. Res.*, 103, 12,869–12,883.
- Wilkin, J. L., M. M. Bowen, and W. J. Emery (2002), Mapping mesoscale currents by optimal interpolation of satellite radiometer and altimeter data, *Ocean Dyn.*, 52, 95–103.

J. L. Wilkin and W. G. Zhang, Institute of Marine and Coastal Sciences, Rutgers, The State University of New Jersey, 71 Dudley Road, New Brunswick, NJ 08901-8521, USA. (wilkin@marine.rutgers.edu)